X-RAY SPECTRAL CONSTRAINTS FOR $z \approx 2$ MASSIVE GALAXIES: THE IDENTIFICATION OF REFLECTION-DOMINATED ACTIVE GALACTIC NUCLEI

D. M. Alexander[1], F. E. Bauer[2,3], W. N. Brandt[4,5], E. Daddi[6], R. C. Hickox[1,7], B. D. Lehmer[8,9], B. Luo[4,5], Y. Q. Xue[4,5],
M. Young[4,5], A. Comastri[10], A. Del Moro[1], A. C. Fabian[11], R. Gilli[10], A. D. Goulding[1,7], V. Mainieri[12],
J. R. Mullaney[1,6], M. Paolillo[13], D. A. Rafferty[4], D. P. Schneider[4], O. Shemmer[14], and C. Vignali[15]

[1] Department of Physics, Durham University, Durham DH1 3LE, UK
[2] Departamento de Astronomía y Astrofísica, Pontificia Universidad Católica de Chile, Casilla 306, Santiago 22, Chile
[3] Space Science Institute, 4750 Walnut Street, Suite 205, Boulder, CO 80301, USA
[4] Department of Astronomy and Astrophysics, 525 Davey Lab, Pennsylvania State University, University Park, PA 16802, USA
[5] Institute for Gravitation and the Cosmos, The Pennsylvania State University, University Park, PA 16802, USA
[6] Laboratoire AIM, CEA/DSM-CNRS-Universite Paris Diderot, Irfu/SAp, Orme des Merisiers, F-91191 Gif-sur-Yvette, France
[7] Harvard-Smithsonian Center for Astrophysics, 60 Garden Street, Cambridge, MA 02138, USA
[8] The Johns Hopkins University, Homewood Campus, Baltimore, MD 21218, USA
[9] NASA Goddard Space Flight Centre, Code 662, Greenbelt, MD 20771, USA
[10] INAF-Osservatorio Astronomico di Bologna, Via Ranzani 1, I-04127 Bologna, Italy
[11] Institute of Astronomy, Madingley Road, Cambridge CB3 0HA, UK
[12] European Southern Observatory, Karl-Schwarzschild-Strasse 2, D-85748 Garching, Germany
[13] Dipartimento di Scienze Fisiche, Universita di Napoli "Federico II," Complesso Universitario di Monte S. Angelo V. Cinthia, 9, I-80126 Napoli, Italy
[14] Department of Physics, University of North Texas, Denton, TX 76203, USA
[15] Dipartimento di Astronomia, Universita degli Studi di Bologna, Via Ranzani 1, 40127 Bologna, Italy

ABSTRACT

We use the 4 Ms *Chandra* Deep Field-South (CDF-S) survey to place direct constraints on the ubiquity of $z \approx 2$ heavily obscured active galactic nuclei (AGNs) in $K < 22$ BzK-selected galaxies. Forty-seven ($\approx 21\%$) of the 222 BzK-selected galaxies in the central region of the CDF-S are detected at X-ray energies, 11 ($\approx 5\%$) of which have hard X-ray spectral slopes ($\Gamma \lesssim 1$), indicating the presence of heavily obscured AGN activity ($N_H \gtrsim 3 \times 10^{23}$ cm^{-2}). The other 36 X-ray detected BzK galaxies appear to be relatively unobscured AGNs and starburst galaxies; we use X-ray variability analyses over a rest-frame baseline of ≈ 3 years to further confirm the presence of AGN activity in many of these systems. The majority (7 out of 11) of the heavily obscured AGNs have excess infrared emission over that expected from star formation (termed "infrared-excess galaxies"). However, we find that X-ray detected heavily obscured AGNs only comprise $\approx 25\%$ of the infrared-excess galaxy population, which is otherwise composed of relatively unobscured AGNs and starburst galaxies. We find that the typical X-ray spectrum of the heavily obscured AGNs is better characterized by a pure reflection model than an absorbed power-law model, suggesting extreme Compton-thick absorption ($N_H \gtrsim 10^{24}$ cm^{-2}) in some systems. We verify this result by producing a composite rest-frame 2–20 keV spectrum, which has a similar shape as a reflection-dominated X-ray spectrum and reveals an emission feature at rest-frame energy ≈ 6.4 keV, likely to be due to Fe K. These heavily obscured AGNs are likely to be the distant analogs of the reflection-dominated AGNs recently identified at $z \approx 0$ with >10 keV observatories. On the basis of these analyses, we estimate the space density for typical (intrinsic X-ray luminosities of $L_{2-10\,\mathrm{keV}} \gtrsim 10^{43}$ erg s^{-1}) heavily obscured and Compton-thick AGNs at $z \approx 2$. Our space-density constraints are conservative lower limits but they are already consistent with the range of predictions from X-ray background models.

Key words: galaxies: active – galaxies: high-redshift – infrared: galaxies – ultraviolet: galaxies – X-rays: galaxies

Online-only material: color figures

1. INTRODUCTION

Deep X-ray surveys have provided a penetrating probe of active galactic nuclei (AGNs) out to $z \approx 5$ (e.g., Brandt & Hasinger 2005; Silverman et al. 2008; Brusa et al. 2009; Brandt & Alexander 2010), identifying obscured and unobscured AGN activity in a modest fraction of the field-galaxy population ($\gtrsim 5\%$–10%; e.g., Lehmer et al. 2005, 2008; Xue et al. 2010). However, there is overwhelming evidence that a large fraction of the heavily obscured AGN population ($N_H \gtrsim 3 \times 10^{23}$ cm^{-2}) remains undetected in even the deepest X-ray surveys (e.g., Worsley et al. 2005; Hickox & Markevitch 2006; Tozzi et al. 2006; Treister et al. 2006; see Section 1 of Alexander et al. 2008). Distant heavily obscured AGNs are predicted by many theoretical models and simulations to represent an important

phase in the evolution of distant dust-enshrouded galaxies, where the rapidly growing central supermassive black hole (BH) is hidden from view (e.g., Fabian 1999; Granato et al. 2006; Hopkins et al. 2006). Therefore, the identification of the most heavily obscured AGNs could be more than just a bookkeeping exercise—without having observations sensitive to their identification we may miss a crucial BH growth phase.

Weak (faint or undetected) X-ray emission from luminous AGNs is likely to be due to the presence of large amounts of dust/gas, sometimes exceeding $N_H \gtrsim 10^{24}$ cm^{-2} (i.e., Compton thick; e.g., Matt et al. 2000; Comastri 2004; Della Ceca et al. 2008; Murphy & Yaqoob 2009). Strong support for this statement comes from the tight correlation between the optical and X-ray emission of unobscured quasars (e.g., Vignali et al. 2003; Steffen et al. 2006; Gibson et al. 2008), which suggests

that all luminous AGNs are *intrinsically* bright at X-ray energies. Although weak at X-ray energies, these heavily obscured AGNs should still be detected in deep mid-to-far-infrared (IR; rest-frame wavelength $>2\,\mu$m) observations due to the presence of dust heated by the hidden AGN. Indeed, a number of studies have revealed large populations of X-ray undetected IR-bright galaxies at $z \approx 2$, which may host heavily obscured, potentially Compton thick, AGN activity (e.g., Daddi et al. 2007a; Fiore et al. 2008, 2009; Georgantopoulos et al. 2008, 2011; Treister et al. 2009b; Georgakakis et al. 2010). Many of these studies have employed X-ray stacking analyses of X-ray undetected IR galaxies to identify hidden AGN populations statistically, where the detection of a hard X-ray spectral slope ($\Gamma \lesssim 1$) in the stacked data provides compelling evidence for the presence of heavily obscured AGN activity in at least a fraction of the stacked sources.[16] Under the assumption that all of these X-ray undetected IR galaxies host Compton-thick AGN activity, the implied space density of these hidden AGNs would exceed those of the Compton-thin AGN population by a factor of $\gtrsim 2$, implying that a much larger fraction of distant luminous AGNs are Compton thick than found locally ($\lesssim$25%–50% of local AGNs appear to be Compton thick; see Table 2 in Burlon et al. 2010; Risaliti et al. 1999; Guainazzi et al. 2005). These discoveries provide some support for the hypothesis that the majority of distant BH growth was more heavily obscured than that found locally (e.g., La Franca et al. 2005; Treister & Urry 2006; Hasinger 2008).

However, results from X-ray stacking analyses need to be treated with caution since they only provide an average signal, leaving significant uncertainties about the overall distribution of source properties. Therefore, before strong conclusions can be derived from these studies, at least two key questions need to be addressed: (1) what fraction of the X-ray stacked signal is "contaminated" by star-forming galaxies, which are found to comprise at least a fraction of the candidate heavily obscured AGN population (e.g., Donley et al. 2008; Murphy et al. 2009; Fadda et al. 2010)? (2), and what fraction of the heavily obscured AGNs are absorbed by Compton-thick (as opposed to Compton-thin) material? The most direct way to address these questions is with deeper X-ray data, which will (1) reveal the X-ray properties of individual IR-bright galaxies that were previously contributing to the stacked X-ray signal, (2) allow for more detailed X-ray spectral investigations of the X-ray detected IR-bright galaxies to search for the signatures of heavily obscured and Compton-thick absorption (e.g., the identification of a strong reflection component at rest-frame >10 keV; the detection of a high equivalent width Fe K emission line; e.g., Matt et al. 1996, 2000; Tozzi et al. 2006; Georgantopoulos et al. 2009; Comastri et al. 2011; Feruglio et al. 2011; see Murphy & Yaqoob 2009),[17] and (3) improve stacking constraints of X-ray undetected populations. The presence of large amounts of absorption can also be indirectly inferred from the identification of luminous AGN emission lines and an IR-emitting hot-dust AGN continuum in X-ray weak systems (e.g., Bassani et al. 1999; Krabbe et al. 2001; Lutz et al. 2004; Alexander et al.

2005b, 2008; Heckman et al. 2005; Gandhi et al. 2009; Bauer et al. 2010; Donley et al. 2010; Gilli et al. 2010; Vignali et al. 2010; Goulding et al. 2011). Greater reliability in the identification of heavily obscured and Compton-thick AGNs is made when considering multiple diagnostics that cross check each other, particularly those that probe different AGN regions.

In this paper, we use the deepest X-ray observations available (the 4 Ms *Chandra* exposure of the *Chandra* Deep Field-South; CDF-S; Xue et al. 2011) to extend the analyses of Daddi et al. (2007a), which employed X-ray stacking techniques to study X-ray undetected IR-bright $z \approx 2$ galaxies in the shallower 1 Ms CDF-S observations. Daddi et al. (2007b) utilized the BzK photometric-selection technique (Daddi et al. 2004) to identify $K < 22$ galaxies at $z \approx 1.4$–2.6 and classified objects based on the ratio of mid-IR ($24\,\mu$m) to extinction-corrected ultraviolet (UV; rest-frame 1500 Å) star formation rates (SFRs). The BzK photometric-selection technique provides an effective identification of massive galaxies ($\approx 10^{10}$–$10^{11}\,M_\odot$; see Daddi et al. 2007b; McCracken et al. 2010). BzK galaxies with a significant excess of IR emission over that predicted from the extinction-corrected UV SFRs were classified as "IR-excess' galaxies" [log(SFR(mid-IR+UV)/SFR(UV,corr)) >0.5], while BzK galaxies with comparable mid-IR and extinction-corrected UV SFRs were classified as "IR-normal galaxies" [log(SFR(mid-IR+UV)/SFR(UV,corr)) $\leqslant 0.5$]. From stacking the X-ray data of the X-ray undetected galaxies, Daddi et al. (2007a) obtained distinctly different X-ray spectral slopes for the IR-excess galaxies ($\Gamma \approx 0.9$) and IR-normal galaxies ($\Gamma \approx 1.8$). The flat X-ray spectral slope found for the IR-excess galaxies indicates that a fraction of the X-ray undetected IR-excess galaxy population host heavily obscured AGN activity, some of which may be Compton thick; by comparison, the stacked X-ray emission from the X-ray undetected IR-normal galaxies is consistent with that expected from star formation. Under the assumption that all of the IR-excess galaxies are Compton-thick AGNs, Daddi et al. (2007a) estimated a space density of $\Phi \approx 2.6 \times 10^{-4}$ Mpc^{-3} for $z \approx 2$ Compton-thick AGNs with $L_{2-10\,{\rm keV}} > 10^{42}$–$10^{43}$ erg s^{-1}. With the deeper *Chandra* data from Xue et al. (2011), we can now better characterize the X-ray properties of both the X-ray detected and X-ray undetected BzK galaxies and improve constraints on the ubiquity of distant heavily obscured and Compton-thick AGNs. We adopt $H_0 = 71$ km s^{-1} Mpc^{-1}, $\Omega_M = 0.27$, and $\Omega_\Lambda = 0.73$ throughout. The Galactic absorption toward the CDF-S region is $N_{\rm H} = 8.8 \times 10^{19}$ cm^{-2} (Stark et al. 1992). All given magnitudes are based on the Vega-magnitude system.

2. DATA AND STACKING PROCEDURES

2.1. Galaxy Sample

We use an updated version of the $z \approx 2$ galaxy samples generated by Daddi et al. (2007b) in the CDF-S field. Due to small refinements in the optical–mid-IR photometry and revised redshift estimates, our updated sample is slightly different to that used in Daddi et al. (2007a, 2007b). However, qualitatively, these samples are the same as those used in Daddi et al. (2007a, 2007b) and have the same global properties.

To provide a good compromise between excellent X-ray sensitivity and a large number of galaxies, we have only explored the X-ray properties of BzK galaxies that lie within $5.'5$ of the average *Chandra* aimpoint. Within this region there are 76 objects classified as IR-excess galaxies and 146 objects classified as IR-normal galaxies.

---

[16] The spectral slopes of X-ray emission from star formation processes are typically $\Gamma \gtrsim 1$ (e.g., Kim et al. 1992; Ptak et al. 1999; Berghea et al. 2008; Iwasawa et al. 2009).

[17] We note that high signal-to-noise ratio (S/N) data are required to accurately distinguish between the X-ray spectral properties of Compton-thin AGNs with $N_{\rm H} \approx (5$–$10) \times 10^{23}$ cm^{-2} and Compton-thick AGNs with $N_{\rm H} \gtrsim 10^{24}$ cm^{-2} (e.g., Murphy & Yaqoob 2009; Yaqoob et al. 2010). Therefore, our adopted definition of a Compton-thick AGN is not comprehensive but is conventional; see the MYTorus manual at www.mytorus.com for a detailed review.

2.2. X-Ray Matching

We matched the parent BzK galaxy sample of 222 objects to the 4 Ms *Chandra* catalogs of Xue et al. (2011) using a $1''\!.5$ search radius. In total, 47 BzK galaxies have an X-ray counterpart, 28 of which are classified as IR-excess galaxies and 19 of which are classified as IR-normal galaxies. The median X-ray–K-band position offset is $0''\!.4$, which agrees with the median uncertainty of the X-ray source positions (which correspond to the 68% confidence level; see Figure 6(a) and Equation (2) in Xue et al. 2011); on the basis of our matching parameters we expect ≈ 1.6 spurious matches. Twenty of these BzK galaxies were detected in the 1 Ms CDF-S catalogs of Alexander et al. (2003) and a further 27 are now detected in the 4 Ms CDF-S catalogs of Xue et al. (2011). The properties of the X-ray detected BzK galaxies are presented in Table 1.

Thirty of the X-ray detected BzK galaxies have spectroscopic redshifts: 27 from optical spectroscopy (predominantly from Very Large Telescope observations with the FORS1, FORS2, and VIMOS instruments; Appenzeller et al. 1998; Le Fèvre et al. 2003) and 3 from *Spitzer*-IRS mid-IR spectroscopy; see Table 1 for the spectroscopic-redshift references. The median spectroscopic redshift is $z_{\rm spec} = 1.78 \pm 0.35$.[18] The other 17 X-ray detected BzK galaxies have photometric redshifts and a median redshift of $z_{\rm photo} = 2.18 \pm 0.50$; see Table 1 for the photometric-redshift references. The median absolute uncertainty between the photometric and spectroscopic redshifts for the X-ray sources with spectroscopic redshifts is $|\Delta z|/(1 + z_{\rm spec}) = 0.02$, where $\Delta z = z_{\rm photo} - z_{\rm spec}$; we get comparable results if we use the Cardamone et al. (2010) photometric-redshift catalog ($|\Delta z|/(1 + z_{\rm spec}) = 0.02$).

2.3. X-Ray Spectroscopy

We extracted and analyzed the X-ray spectra of the X-ray detected BzK galaxies to provide greater insight into their intrinsic properties. The X-ray spectra were extracted using ACIS_EXTRACT (Broos et al. 2010) as part of the X-ray catalog construction in Xue et al. (2011); see Section 3.2 of Xue et al. (2011) for more details.

Due to the limited counting statistics for the majority of the heavily obscured AGNs ($\lesssim 80$ counts in the 0.5–8 keV band; see Table 2), which are the primary focus of this paper, the X-ray spectral analyses were predominantly performed using the C-statistic (Cash 1979). The C-statistic is calculated on the unbinned data and is therefore ideally suited to low-count sources (e.g., Nousek & Shue 1989). However, to provide consistency checks on these results, we also performed X-ray spectral analyses of the brightest X-ray sources (>200 counts in the 0.5–8 keV band) using χ^2 statistics; in these analyses we grouped the X-ray data into 20 counts per bin. All fit parameter uncertainties are quoted at the 90% confidence level (Avni 1976).

2.4. X-Ray Variability

We analyzed the X-ray variability of the X-ray detected BzK galaxies to look for nuclear activity. The CDF-S observations were split into four epochs, each approximately 1 Ms long: 2000, 2007, 2010a (March–May), and 2010b (May–July). Within each epoch, the observations were merged and photometry was

measured using ACIS_EXTRACT (Broos et al. 2010), as described in detail in Xue et al. (2011).

We apply a χ^2 test to determine if a source is variable by comparing the variability observed between observations to that expected from Poisson statistics. The test statistic will follow a χ^2 distribution except at low count rates, where the errors are larger than expected from a Gaussian distribution. In the low-count regime, the test statistic is smaller than expected and does not follow the χ^2 distribution. We construct a Monte Carlo simulation to determine what distribution the test statistic should follow for each source, following the procedure of Paolillo et al. (2004). The observed test statistic is compared to the simulated distribution to determine the probability (P_{χ^2}) that the observed variability is due to Poisson noise. The χ^2 and P_{χ^2} values are listed in Table 2. A source is considered variable if it has >20 counts in the 0.5–8 keV band and $P_{\chi^2} < 5\%$.

The normalized excess variance ($\sigma^2_{\rm rms}$; Nandra et al. 1997) measures how strongly each source varies in excess of measurement error. Since it is more likely that a variable galaxy harbors an AGN if the observed variability exceeds that expected from a population of X-ray binaries, we estimate the amount of variability expected from high-mass X-ray binaries (HMXBs). HMXB variability can be estimated from a galaxy's SFR (see Figure 8 of Gilfanov et al. 2004). To use this relation we adopt $\sigma^2_{\rm rms} = 0.09$ as the typical variability for an individual X-ray binary (equivalent to 30% fractional rms; see Section 6 of Gilfanov 2010). This value is the maximum variability expected for an HMXB population. Variability strength will increase with the length of the timescale over which it is measured (e.g., Nandra et al. 1997); hence adopting the maximum HMXB variability is appropriate for CDF-S sources at $z \approx 2$, where rest-frame timescales are ≈ 3 years. The SFR of the BzK galaxies was estimated from their UV and IR luminosities (Xue et al. 2010). Applying the $\sigma^2_{\rm rms}$–SFR relations (Gilfanov et al. 2004), we calculate an upper limit to the HMXB contribution to the variability, reported as $\sigma^2_{\rm HMXB}$ in Table 2. A source is considered to be an X-ray variable AGN if it is found to be variable, as prescribed above, and also has excess variability over that expected from HMXBs. On the basis of these criteria, 13 of the 27 sources with >20 counts in the 0.5–8 keV band are found to be variable AGN.

2.5. X-Ray Stacking Analyses

We used X-ray stacking analyses to constrain the average X-ray properties of the X-ray undetected BzK galaxy populations. In our X-ray stacking analyses we adopted the procedure of Lehmer et al. (2008), which takes a different approach from the Worsley et al. (2005) method used by Daddi et al. (2007a). Both procedures stack the X-ray data of the selected sources but Lehmer et al. (2008) determine the background counts using large source-free apertures local to each source, while Worsley et al. (2005) determine the background counts from a large number of randomly placed apertures around the source (i.e., a Monte Carlo approach). We tested both procedures on our data sets and achieved statistically consistent results. The major advantage of the Lehmer et al. (2008) approach over that of Worsley et al. (2005) is computational speed. In the stacking analyses, we used a fixed aperture of $1''\!.5$ radius and determined background counts in $25'' \times 25''$ source-free regions local to each source. We applied aperture corrections to the net stacked count rates following Section 4.2 in Lehmer et al. (2008).

A general concern in stacking analyses is that a few sources can dominate the stacked signal. To guard against this, we randomly selected 80% of the objects in each stacking analysis

---

[18] The error on the median is the median absolute deviation (MAD), which is a robust estimator of the spread of the sample: $\mathrm{MAD} = 1.48 \times \mathrm{median}(|x - \mathrm{median}(x)|)$; see Section 1.2 of Maronna et al. (2006).

Table 1
Overall Properties of the X-Ray Detected *BzK* Galaxies

K-band		X–K	K_Vega			L_{UV}	$L_{2-10\,keV}$	$vL_{8\,\mu m}$	SFR	Γ^d	1 Ms	Notes[f]
α_{J2000}[a]	δ_{J2000}[a]	(arcsec)[b]	z^c	(mag)[a]	XID[d]	$\log(L_\odot)$[a]	$\log(erg\,s^{-1})$[d]	$\log(L_\odot)$[a]	Excess[a]		Source?[e]	
03 32 10.95	−27 48 56.1	0.48	2.81	20.2	167	12.04	43.96	11.72	17.3	$1.68^{+0.08}_{-0.09}$	Y	
03 32 12.55	−27 49 38.2	0.29	2.45	21.3	185	11.54	42.14	10.64	1.3	> 0.53	N	
03 32 14.12	−27 49 10.2	0.59	2.18	20.6	202	11.33	42.06	11.20	15.0	> 0.57	N	
03 32 14.42	−27 51 10.7	0.39	1.544	19.2	205	12.11	41.98	10.72	0.5	$0.13^{+0.23}_{-0.20}$	Y	Heavily obscured AGN; optical AGN
03 32 14.79	−27 44 02.5	0.67	1.56	20.7	208	10.80	42.33	10.37	2.9	$1.25^{+0.40}_{-0.29}$	N	
03 32 16.94	−27 50 04.0	0.35	1.613	20.6	236	11.40	41.59	10.50	1.1	> 0.60	N	
03 32 17.81	−27 52 10.3	0.57	1.76	21.7	247	10.98	<41.95	10.47	2.7	−	N	
03 32 18.24	−27 52 41.2	0.45	2.801	21.4	254	11.35	43.41	10.74	2.9	$1.79^{+0.26}_{-0.20}$	Y	Optical AGN
03 32 21.30	−27 51 01.5	0.52	1.84	20.2	293	11.70	41.68	11.10	4.5	$0.36^{+0.64}_{-0.44}$	N	Heavily obscured AGN
03 32 21.99	−27 51 11.9	0.28	3.64	21.2	298	11.39	42.76	11.85	124.6	$0.01^{+0.21}_{-0.19}$	Y	Heavily obscured AGN
03 32 22.54	−27 46 03.8	0.44	1.730	20.4	308	11.26	42.90	11.00	8.7	$0.17^{+0.07}_{-0.06}$	Y	Heavily obscured AGN
03 32 22.55	−27 48 14.9	0.48	2.54	20.4	310	11.63	41.90	11.20	7.4	$-0.59^{+0.26}_{0.22}$	N	Heavily obscured AGN
03 32 24.84	−27 50 50.1	0.38	2.28	20.7	337	11.47	41.91	11.14	8.7	> 0.43	N	
03 32 25.98	−27 47 51.3	0.69	1.90i	20.5	360	11.47	41.91	11.12	8.0	> 0.94	N	IRS: s/burst dominated
03 32 28.79	−27 47 55.5	0.95	1.383	19.3	394	12.07	41.59	10.75	0.6	> 0.64	N	
03 32 29.09	−27 46 29.0	0.34	2.227	19.8	399	11.89	41.91	11.27	5.2	> 0.42	N	
03 32 29.48	−27 43 22.0	0.56	1.609	19.8	405	11.66	<41.90	10.66	1.1	< 0.09	N	Heavily obscured AGN
03 32 29.99	−27 45 29.9	0.38	1.218	18.3	417	11.69	43.74	11.03	3.6	$1.44^{+0.04}_{-0.04}$	Y	Optical AGN
03 32 31.47	−27 46 23.2	0.43	2.223	19.0	435	12.41	42.43	11.71	7.2	$1.00^{+0.32}_{-0.27}$	Y	Heavily obscured AGN
03 32 31.52	−27 48 53.8	0.43	1.879	20.3	437	11.66	42.41	11.25	8.3	$1.31^{+0.34}_{-0.27}$	Y	IRS: s/burst dominated
03 32 31.55	−27 50 28.6	0.76	1.613	18.9	436	12.14	<41.64	11.01	1.2	< 0.70	N	Heavily obscured AGN
03 32 32.93	−27 50 40.5	0.82	2.50	20.5	451	11.96	41.92	11.08	2.3	> 0.23	N	
03 32 34.04	−27 50 28.7	0.44	1.384	19.5	467	11.76	41.42	10.71	1.0	> 0.46	N	
03 32 34.46	−27 50 04.9	0.21	2.14	20.5	474	11.46	41.99	11.41	22.5	> 0.77	N	
03 32 34.98	−27 49 31.9	0.97	2.55	21.9	481	11.44	42.03	11.30	16.1	> 0.51	Y	
03 32 35.72	−27 49 16.1	0.31	2.578	20.0	490	11.85	42.51	12.25	171.0	$0.44^{+0.23}_{-0.20}$	Y	Heavily obscured AGN; optical AGN
03 32 35.97	−27 48 50.4	0.31	1.309	19.1	493	11.93	42.24	10.55	0.4	$1.98^{+0.43}_{-0.34}$	Y	
03 32 36.17	−27 51 26.5	0.37	1.613	20.0	499	11.69	42.67	10.80	1.6	$1.27^{+0.18}_{0.16}$	Y	
03 32 36.18	−27 46 27.6	0.43	2.48	20.9	501	11.96	41.99	11.03	1.9	> 0.41	N	
03 32 37.36	−27 46 45.5	0.62	1.843	20.0	512	11.71	41.74	11.00	3.0	> 0.42	N	
03 32 37.74	−27 50 00.6	0.81	1.619	19.2	517	12.23	41.71	11.16	1.6	> 0.64	N	
03 32 37.77	−27 52 12.3	0.27	1.603	18.8	518	11.98	44.16	11.64	15.1	$1.71^{+0.03}_{-0.03}$	Y	Optical AGN; IRS: AGN dominated
03 32 37.96	−27 53 07.9	0.26	1.97	21.2	520	11.44	42.60	10.55	1.2	> 1.41	Y	
03 32 38.55	−27 46 34.2	0.77	2.55i	21.3	525	11.68	42.27	11.77	46.7	> 0.86	N	IRS: s/burst dominated
03 32 39.08	−27 46 02.1	0.17	1.216	18.3	537	11.85	43.22	10.82	1.2	$1.13^{+0.05}_{-0.05}$	Y	Optical AGN
03 32 39.74	−27 46 11.5	0.08	1.552	19.4	549	11.63	43.24	11.08	4.9	$1.16^{+0.07}_{-0.07}$	Y	IRS: s/burst dominated
03 32 40.06	−27 47 55.4	0.45	1.998	19.5	552	12.08	41.99	11.58	9.8	> 0.63	N	IRS: s/burst dominated
03 32 40.76	−27 49 26.2	0.40	2.130	19.7	555	11.85	42.05	11.34	7.2	> 0.65	N	IRS: s/burst dominated
03 32 41.80	−27 51 35.3	0.20	1.63	20.2	562	11.54	41.90	10.94	3.7	$0.77^{+0.57}_{-0.38}$	N	Heavily obscured AGN
03 32 43.25	−27 49 14.3	0.20	1.920	19.5	577	11.31	43.96	11.10	10.9	$1.55^{+0.04}_{-0.04}$	Y	Optical AGN
03 32 43.46	−27 49 01.8	0.46	1.78i	20.2	579	11.76	42.00	11.27	7.0	> 0.88	Y	IRS: s/burst dominated
03 32 43.61	−27 46 59.0	0.20	1.570	20.4	580	11.46	41.86	10.66	1.7	> 0.83	N	
03 32 44.02	−27 46 34.9	1.00	2.688	20.9	583	11.75	43.63	11.69	31.1	$2.00^{+0.15}_{-0.16}$	Y	IRS: s/burst dominated
03 32 44.37	−27 49 11.3	0.53	2.13	20.4	589	11.25	<42.03	11.44	40.5	> 0.60	N	
03 32 44.60	−27 48 36.0	0.18	2.593	21.4	593	11.55	43.38	11.11	6.6	$1.19^{+0.12}_{-0.11}$	Y	
03 32 46.84	−27 51 20.9	0.25	2.292	20.4	617	11.74	42.42	11.06	3.6	> 0.73	N	
03 32 47.72	−27 50 38.0	0.40	1.63	19.2	625	12.06	41.94	11.21	2.8	$-0.33^{+0.20}_{-0.19}$	N	Heavily obscured AGN

Notes. [a] *BzK* galaxy properties taken from Daddi et al. (2007b). Coordinates correspond to the *K*-band position of the *BzK* galaxy. The UV luminosity corresponds to rest-frame 1500 Å and has been corrected for extinction (see Section 3.6 of Daddi et al. 2007b). The rest-frame 8 μm luminosity is calculated using the 24 μm flux density, with small *K*-corrections applied (see Section 3.1 of Daddi et al. 2007b). The SFR excess corresponds to the ratio of star formation rates (mid-IR+UV vs. extinction-corrected UV; see Section 2.2 of Daddi et al. 2007a).
[b] Offset between the position of the X-ray source and the *K*-band *BzK* counterpart in arcseconds.
[c] *BzK* galaxy redshifts. Optical spectroscopic redshifts are denoted by having three decimal places and come from Szokoly et al. (2004), Mignoli et al. (2005), Cimatti et al. (2008), Vanzella et al. (2008), Popesso et al. (2009), and Balestra et al. (2010). All other redshifts are either photometric (from Grazian et al. 2006; Luo et al. 2010; Rafferty et al. 2011) or from *Spitzer*-IRS spectroscopy (highlighted with "i" and from Teplitz et al. 2007 and Fadda et al. 2010).
[d] X-ray source properties. XID corresponds to the X-ray identification number in Xue et al. (2011). The X-ray spectral slope (Γ) determined from the band ratio (2–8 keV to 0.5–2 keV count-rate ratio) plus 1σ uncertainty are taken from Xue et al. (2011); Γ is re-calculated from the band ratio for the low-count sources listed in Xue et al. (2011) with Γ = 1.4. The rest-frame 2–10 keV luminosity is calculated from the observed-frame 0.5–2 keV flux in Xue et al. (2011) and converted to rest-frame 2–10 keV assuming Γ = 1.8.
[e] Indicates if the source was detected in the 1 Ms CDF-S catalogs of Alexander et al. (2003); otherwise, the source was detected in the 4 Ms CDF-S catalogs of Xue et al. (2011).
[f] Notes and classifications. Objects classified as "Heavily obscured AGN" have Γ $\lesssim$ 1 and objects classified as optical AGN have optical spectroscopic signatures from Szokoly et al. (2004) indicating AGN activity. We have also indicated which sources have *Spitzer*-IRS spectroscopy, available either from Teplitz et al. (2007), Donley et al. (2010), or Fadda et al. (2010).

Table 2
X-Ray Properties of the X-Ray Detected BzK Galaxies

X-Ray		Net Counts[b]	X-Ray Variability Constraints[c]				Variable
$\alpha_{\rm J2000}$[a]	$\delta_{\rm J2000}$[a]		χ^2	P_{χ^2}	$\sigma_{\rm rms}^2$	$\sigma_{\rm HMXB}^2$	AGN?[d]
03 32 10.98	$-27\ 48\ 56.5$	844	4.09	0.004	0.014	0.0054	Y
03 32 12.57	$-27\ 49\ 38.2$	9	...	...	...	...	...
03 32 14.15	$-27\ 49\ 10.6$	18	...	...	...	...	...
03 32 14.43	$-27\ 51\ 11.0$	82	4.30	0.005	0.141	0.0011	Y
03 32 14.80	$-27\ 44\ 03.2$	89	0.371	0.723	-0.034	N/A	N
03 32 16.96	$-27\ 50\ 04.2$	5	...	...	...	...	...
03 32 17.84	$-27\ 52\ 10.8$	27	0.952	0.289	-0.001	0.0030	N
03 32 18.24	$-27\ 52\ 41.6$	215	1.46	0.183	0.009	0.0019	N
03 32 21.31	$-27\ 51\ 02.0$	22	0.688	0.416	-0.092	0.0110	N
03 32 22.00	$-27\ 51\ 12.1$	80	0.106	0.952	-0.058	0.0110	N
03 32 22.56	$-27\ 46\ 04.2$	564	6.47	0.000	0.036	0.0005	Y
03 32 22.58	$-27\ 48\ 15.2$	58	0.228	0.842	-0.073	0.0110	N
03 32 24.85	$-27\ 50\ 50.4$	7	...	...	...	...	...
03 32 26.01	$-27\ 47\ 51.8$	8	...	...	...	...	...
03 32 28.85	$-27\ 47\ 56.0$	17	...	...	...	...	...
03 32 29.11	$-27\ 46\ 29.3$	12	...	...	...	...	...
03 32 29.50	$-27\ 43\ 22.5$	54	0.682	0.451	-0.038	N/A	N
03 32 29.99	$-27\ 45\ 30.3$	3916	130	0.000	0.163	0.0003	Y
03 32 31.48	$-27\ 46\ 23.6$	59	0.870	0.352	-0.017	0.0000	N
03 32 31.55	$-27\ 48\ 54.0$	61	0.670	0.481	-0.046	0.0081	N
03 32 31.51	$-27\ 50\ 29.0$	16	...	...	...	...	...
03 32 32.95	$-27\ 50\ 41.3$	10	...	...	...	...	...
03 32 34.03	$-27\ 50\ 29.1$	12	...	...	...	...	...
03 32 34.47	$-27\ 50\ 05.1$	10	...	...	...	...	...
03 32 35.04	$-27\ 49\ 32.5$	4	...	...	...	...	...
03 32 35.72	$-27\ 49\ 16.4$	70	1.64	0.144	0.019	0.0110	N
03 32 35.98	$-27\ 48\ 50.7$	84	5.26	0.001	0.300	0.0014	Y
03 32 36.18	$-27\ 51\ 26.8$	179	2.13	0.067	0.027	0.0009	N
03 32 36.19	$-27\ 46\ 28.0$	3	...	...	...	...	...
03 32 37.38	$-27\ 46\ 46.1$	11	...	...	...	...	...
03 32 37.75	$-27\ 50\ 01.4$	14	...	...	...	...	...
03 32 37.77	$-27\ 52\ 12.6$	4600	250	0.000	0.021	0.0001	Y
03 32 37.96	$-27\ 53\ 08.2$	71	3.38	0.014	0.141	0.0004	Y
03 32 38.52	$-27\ 46\ 34.9$	14	...	...	...	...	...
03 32 39.09	$-27\ 46\ 02.1$	1331	134	0.000	0.346	0.0005	Y
03 32 39.74	$-27\ 46\ 11.5$	760	0.833	0.453	-0.001	0.0003	N
03 32 40.05	$-27\ 47\ 55.8$	26	1.50	0.145	-0.014	0.0110	N
03 32 40.77	$-27\ 49\ 26.6$	13	...	...	...	...	...
03 32 41.82	$-27\ 51\ 35.4$	37	4.09	0.007	0.508	0.0007	Y
03 32 43.24	$-27\ 49\ 14.5$	2117	39.2	0.000	0.077	0.0004	Y
03 32 43.45	$-27\ 49\ 02.2$	19	...	...	...	...	...
03 32 43.61	$-27\ 46\ 59.2$	16	...	...	...	...	...
03 32 44.04	$-27\ 46\ 35.9$	380	1.13	0.281	0.001	N/A	N
03 32 44.41	$-27\ 49\ 11.3$	7	...	...	...	...	...
03 32 44.61	$-27\ 48\ 36.2$	333	3.40	0.011	0.033	0.0003	Y
03 32 46.86	$-27\ 51\ 21.0$	43	4.34	0.006	0.335	0.0056	Y
03 32 47.73	$-27\ 50\ 38.4$	118	10.4	0.000	0.210	0.0002	Y

Notes. [a] Coordinates correspond to the X-ray position from Xue et al. (2011).
[b] Background-subtracted (net) counts in the 0.5–8.0 keV band used in the X-ray spectral analyses and X-ray variability analyses.
[c] X-ray variability constraints for the sources with reasonable-quality X-ray data (> 20 counts in the 0.5–8 keV band). The χ^2 statistic is calculated by comparing the variability observed between observations to that expected from Poisson statistics. P_{χ^2} gives the probability that the observed variability is due to Poisson noise, $\sigma_{\rm rms}^2$ gives the normalized excess variance (Nandra et al. 1997), and $\sigma_{\rm HMXB}^2$ gives the upper limit to the HMXB contribution to the variability. N/A indicates that no SFR information was available and so no attempt was made to estimate $\sigma_{\rm HMXB}^2$: this does not affect any significantly variable sources. See Section 2.4.
[d] Indicates if the source was found to show excess X-ray variability over that expected from the HMXB population; see Section 2.4.

sample and stacked their properties. For each sample we performed this procedure 10,000 times, randomly selecting 80% of the objects for each iteration, to generate a distribution of the stacked properties. We found that the overall properties obtained from the stacking analyses were in good agreement with the overall properties found from the stacking analysis trials, indicating that bright sources do not dominate the stacked signal.
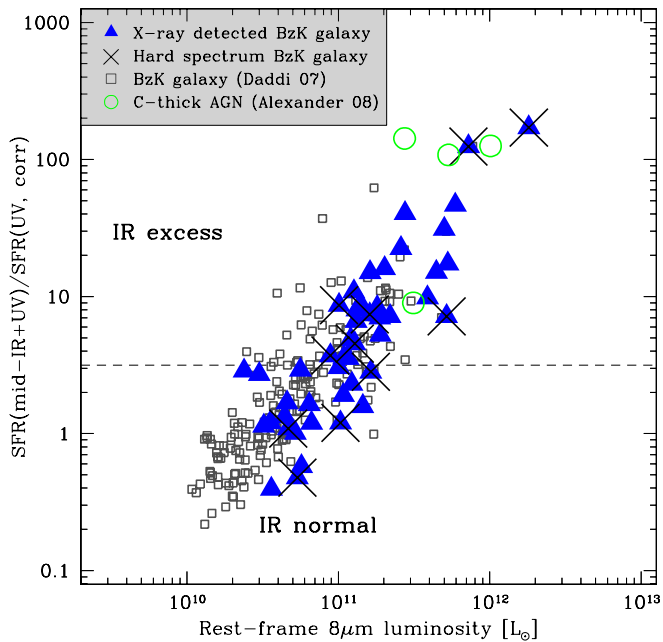
Figure 1. Ratio of star formation rates (SFRs; mid-IR and extinction-corrected UV) for the $z \approx 2$ galaxies studied by Daddi et al. (2007a, 2007b) vs. rest-frame $8\,\mu$m luminosity. Triangles correspond to X-ray detected BzK galaxies, crosses indicate the BzK galaxies with hard X-ray spectral slopes (heavily obscured AGNs; see Figure 2), open squares correspond to the X-ray undetected BzK galaxies, and the open circles correspond to the spectroscopically identified (optical and mid-IR wavelengths) Compton-thick AGNs at $z \approx 2$ from Alexander et al. (2008) in the 2 Ms *Chandra* Deep Field-North survey (Alexander 2003). The threshold between IR excess and IR normal galaxies defined by Daddi et al. (2007a, 2007b) is indicated by the dashed line.

(A color version of this figure is available in the online journal.)

3. ANALYSES AND RESULTS

We focus our analyses toward (1) characterizing the X-ray spectral and variability properties of X-ray detected BzK galaxies to identify the presence of AGN activity (see Section 3.1), and (2) performing X-ray stacking analyses of the X-ray undetected BzK galaxies in the 4 Ms CDF-S observations (see Section 3.2). With the results of these investigations, we re-evaluate estimates of the space density of distant heavily obscured and Compton-thick AGNs (see Section 3.3).

3.1. X-Ray Detected BzK Galaxies

In Figure 1, we compare the properties of the X-ray detected BzK galaxies to the overall BzK galaxy population. The X-ray detected BzK galaxies cover a wide range in SFR ratio (log(SFR(mid-IR+UV)/SFR(UV,corr)) and rest-frame $8\,\mu$m luminosity. However, when compared to the X-ray undetected BzK galaxies, the X-ray detected systems have characteristically higher median SFR ratios and rest-frame $8\,\mu$m luminosities (X-ray detected: SFR ratio of $\approx 4.5 \pm 4.9$ and log($L_{8\,\mu m}/L_{\odot}$) $\approx 11.1 \pm 0.4$; X-ray undetected: SFR ratio of $\approx 1.4 \pm 1.4$ and log($L_{8\,\mu m}/L_{\odot}$) $\approx 10.6 \pm 0.4$).[19] Overall, $\approx 37\%$ of the IR-excess galaxy population and $\approx 13\%$ of the IR-normal galaxy population are now detected in the 4 Ms *Chandra* exposure, indicating a close connection between the production of X-ray emission and the presence of excess (or luminous) IR emission. Indeed, the X-ray detected fraction rises as a function

---

[19] $L_{8\,\mu m} \gtrsim 10^{11}\,L_{\odot}$ is comparable to $L_{\rm IR} \gtrsim 10^{12}\,L_{\odot}$ for the spectral energy distribution corrections adopted in Daddi et al. (2007b).
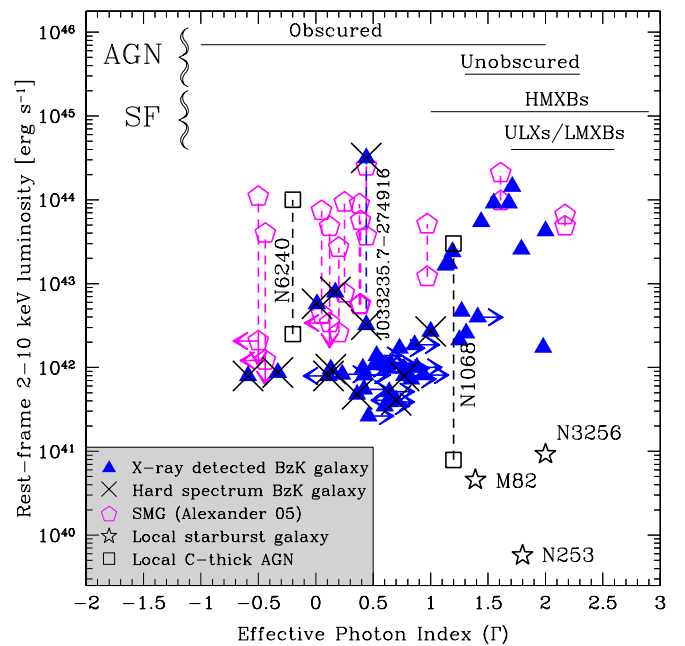
Figure 2. Rest-frame 2–10 keV luminosity vs. X-ray spectral slope (Γ is in the observed-frame 0.5–8 keV, typically rest-frame 1.5–24 keV). The properties of $z \approx 2$ SMGs hosting AGN activity (open pentagons; from Alexander et al. 2005a) and X-ray detected BzK galaxies (filled triangles; identified here) are compared to well-studied local starbursts (open stars) and local Compton-thick AGNs (open squares). The properties of the local starburst galaxies and Compton-thick AGNs are taken from Ranalli et al. (2003), Matt et al. (1997), and Vignati et al. (1999). The vertical dashed lines indicate the difference between the observed X-ray luminosity and the absorption-corrected luminosity for the SMGs and Compton-thick AGNs (from Matt et al. 1997; Vignati et al. 1999; Alexander et al. 2005a; Feruglio et al. 2011); the intrinsic X-ray luminosity constraint for J033235.7–274916 is from Feruglio et al. (2011), which is one of the heavily obscured AGNs in our sample. The range of X-ray spectral slopes found for typical AGNs and star-forming galaxies are illustrated (horizontal solid lines; constraints derived from Kim et al. 1992; Nandra & Pounds 1994; Maiolino et al. 1998; Ptak et al. 1999; Berghea et al. 2008). Eleven of the X-ray detected BzK galaxies have flat X-ray spectral slopes ($\Gamma \lesssim 1$) and are classified as heavily obscured AGNs (crosses).

(A color version of this figure is available in the online journal.)

of rest-frame $8\,\mu$m luminosity: $\approx 3\%$, $\approx 14\%$, and $\approx 51\%$ of the log($L_{8\,\mu m}/L_{\odot}$) = 10.0–10.5, log($L_{8\,\mu m}/L_{\odot}$) = 10.5–11.0, and log($L_{8\,\mu m}/L_{\odot}$) > 11.0 systems are detected at X-ray energies, respectively. Given these results, X-ray observations an order of magnitude deeper than those obtained here (only likely to be attainable with the next generation of X-ray observatories; e.g., *Generation-X*; Wolk et al. 2008) are required to individually detect X-ray emission from the majority of the lowest-luminosity systems.

3.1.1. Classification of the X-Ray Emission

In Figure 2, we plot the rest-frame 2–10 keV luminosity versus X-ray spectral slope of the X-ray detected BzK galaxies and compare them to well-studied local starburst galaxies, Compton-thick AGNs, and $z \approx 2$ submillimeter-emitting galaxies (SMGs) hosting AGN activity; the rest-frame 2–10 keV luminosities are calculated from the observed-frame 0.5–2 keV fluxes assuming $\Gamma = 1.8$ for the small K corrections. Eleven ($\approx 23\%$) of the 47 X-ray detected BzK galaxies have flat X-ray spectral slopes with $\Gamma \lesssim 1$ (eight have $\Gamma \lesssim 0.5$) and are classified here as "heavily obscured AGNs." On the basis of the X-ray properties of the $z \approx 2$ SMGs hosting AGN activity (Alexander et al. 2005a), the flat X-ray spectral slopes for these heavily obscured AGNs
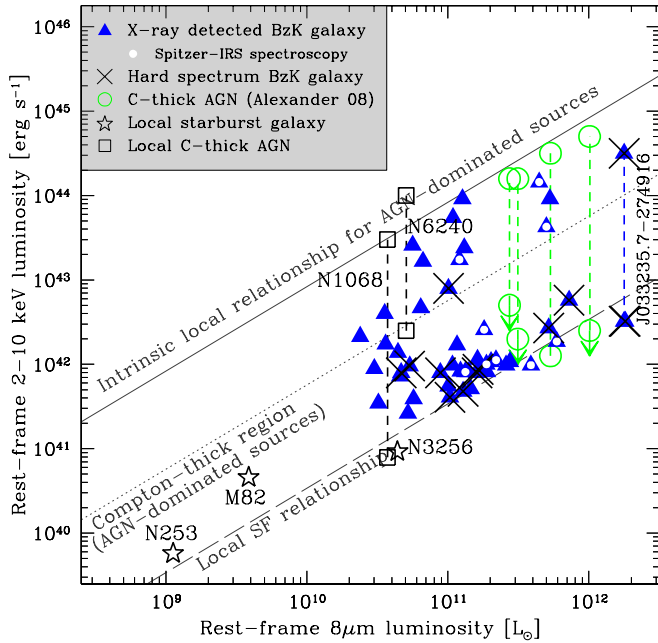
Figure 3. Rest-frame 2–10 keV luminosity vs. rest-frame 8 μm luminosity. The symbols have the same meaning as in Figures 1 and 2; in addition, the small filled circles show the X-ray detected BzK galaxies with *Spitzer*-IRS spectroscopy. The X-ray–8 μm luminosity ratio for local starburst galaxies (long-dashed line) is taken from the X-ray–12 μm luminosity ratio of Krabbe et al. (2001) and converted to 8 μm assuming the M 82 spectral energy distribution. The intrinsic X-ray–8 μm luminosity ratio for local AGNs (solid line) is taken from Lutz et al. (2004) and converted to 8 μm, assuming the AGN-dominated galaxy NGC 1068; the dotted line indicates the observed X-ray–8 μm luminosity ratio predicted for Compton-thick AGNs. The rest-frame 8 μm luminosity for the X-ray detected BzK galaxies is calculated from the 24 μm flux density, with small K-corrections applied (see Daddi et al. 2007a), while the rest-frame 8 μm luminosity for the local starburst galaxies is calculated using the mid-IR spectroscopy of Rigopoulou et al. (1999) and Lutz et al. (2003). The vertical dashed lines indicate the difference between the observed and intrinsic X-ray luminosity for the $z \approx 2$ Compton-thick AGNs from Alexander et al. (2008) and Feruglio et al. (2011); the intrinsic X-ray luminosity constraint for J033235.7–274916 is from Feruglio et al. (2011), which is one of the heavily obscured AGNs in our sample.

(A color version of this figure is available in the online journal.)

suggest absorbing column densities of $N_H \gtrsim 3 \times 10^{23}$ cm^{-2} and some may be Compton thick; see Figure 2. The absorption corrections for such heavily obscured AGNs in the rest-frame 2–10 keV band are large and would imply intrinsic luminosities of $L_{2-10\,keV} \gtrsim 10^{43}$ erg s^{-1}. Six of these heavily obscured AGNs are not detected in the 1 Ms CDF-S data used in Daddi et al. (2007a).

On the basis of the X-ray luminosity and X-ray spectral slope, the X-ray emission from the majority of the other 36 X-ray detected BzK galaxies is likely to be due to either relatively unobscured AGN activity ($N_H \lesssim 10^{22}$–10^{23} cm^{-2}) or star formation. Nine of these objects have $L_X > 10^{43}$ erg s^{-1}, five of which are identified as AGNs based on optical spectroscopy (see Table 1), and are classified here as "luminous AGNs." The other 27 X-ray detected BzK galaxies are likely to be lower-luminosity AGNs or X-ray luminous starbursts and are classified here as "low-luminosity X-ray systems;" as shown in Figure 3 and Section 3.1.2, the X-ray–IR luminosity ratios of these systems are also similar to those expected for starburst galaxies or $z \approx 2$ AGNs with $L_X \approx 10^{42}$–10^{43} erg s^{-1} (e.g., Krabbe et al. 2001; Mullaney et al. 2010; Shao et al. 2010). Twenty-one of

these low-luminosity X-ray systems are not detected in the 1 Ms CDF-S data used in Daddi et al. (2007a).

Four of the 27 low-luminosity X-ray systems are detected in both the 2–8 keV and 0.5–2 keV bands and their X-ray spectral slopes are $\Gamma \approx 1.2$–2.0. The other 23 low-luminosity X-ray systems are undetected at 2–8 keV and we can only provide accurate constraints on their X-ray spectral slopes using X-ray stacking analyses. Stacking the X-ray data for these 23 systems, following the procedure outlined in Section 2.5, we obtain significant detections in both the 2–8 keV (S/N = 8.3) and 0.5–2 keV bands (S/N = 29.7), which correspond to an average X-ray spectral slope of $\Gamma = 1.5 \pm 0.1$. The comparatively steep X-ray spectral slope from this population could be due to either star formation or AGN activity and does not provide significant new insight into the composition of the low-luminosity X-ray systems.

We can further characterize the X-ray detected BzK galaxies using X-ray variability analyses. The identification of significant X-ray variability over that expected from star formation processes will indicate the presence of an AGN; see Section 2.4. Overall, we find that 13 ($\approx$48%) of the 27 X-ray detected BzK galaxies with reasonable-quality X-ray data ($>$20 X-ray counts) show excess variability over that expected from star formation processes; the sources show variability by factors of $\approx$1.4–4.3 (see Table 2). Nine of these 13 systems had already been classified as AGNs: six are luminous AGNs and four are heavily obscured AGNs. However, three of the variable sources are classified as low-luminosity X-ray systems ($\approx$40% of those with reasonable-quality X-ray data), unambiguously identifying the presence of AGNs in at least a fraction of the low-luminosity X-ray systems.

3.1.2. X-Ray–Infrared Properties

In Figure 3, we plot the rest-frame 2–10 keV luminosity versus rest-frame 8 μm luminosity of the X-ray detected BzK galaxies and compare them to well-studied local starburst galaxies and Compton-thick AGNs. This figure can help characterize the X-ray–8 μm luminosity ratio and provide constraints on the intrinsic luminosity of the heavily obscured AGNs. For example, under the assumption that the 8 μm emission is dominated by AGN activity, the X-ray–8 μm luminosity ratios of the heavily obscured AGNs suggest that they have intrinsic X-ray luminosities of $L_{2-10\,keV} \approx 3 \times 10^{43}$–$10^{45}$ erg s^{-1} (see Figure 3). The presence of absorption at 8 μm, as predicted by radiative-transfer modeling of clumpy AGN obscuration (e.g., Nenkova et al. 2008), will increase these intrinsic X-ray luminosity estimates; however, see Lutz et al. (2004) and Gandhi et al. (2009) for observational constraints suggesting that obscured AGNs do not typically suffer significant nuclear absorption at infrared wavelengths. Under the assumption that the 8 μm emission is AGN dominated, the X-ray–8 μm luminosity ratios for all of the heavily obscured AGNs, except for J033222.5–274603, are also consistent with those expected for Compton-thick AGNs.

However, the interpretation of the X-ray–8 μm luminosity ratio is complicated by the absence of mid-IR spectroscopy for the majority of the X-ray detected BzK galaxies, which would directly measure the contributions from star formation and AGN activity at rest-frame 8 μm. Nine of the X-ray detected BzK galaxies have *Spitzer*-IRS spectroscopy, three of which are classified as X-ray luminous AGNs and six of which are classified as low-luminosity X-ray sources; see Table 1 and Figure 3. With the exception of the luminous AGN J033237.7–275212 (which is AGN-dominated at 8 μm; Donley et al. 2010), all

of the other eight systems are star formation dominated at 8 μm, including two of the luminous AGNs (Teplitz et al. 2007; Fadda et al. 2010). If the heavily obscured AGNs are the absorbed counterparts of the luminous AGNs, as suggested by the X-ray spectral analyses (see Section 3.1.3), then we would expect many of them to also be star formation dominated at 8 μm and, therefore, the range of intrinsic X-ray luminosities estimated above ($L_{2-10 \, keV} \approx 3 \times 10^{43}$–$10^{45}$ erg s^{-1}) are upper limits; see Section 3.1.4 for further estimates of the intrinsic X-ray luminosities.

The majority of the heavily obscured AGNs are identified as IR-excess galaxies (7 of the 11 systems); see Figure 1. However, the majority of the X-ray detected IR-excess galaxies are not heavily obscured AGNs: only 7 ($\approx$25%) of the 28 X-ray detected systems are heavily obscured AGNs, 7 ($\approx$25%) are luminous AGNs, and 14 ($\approx$50%) are low-luminosity X-ray systems (one of which has been found to be an X-ray variable AGN: J033246.8–275120; see Tables 1 and 2). This shows that the IR-excess galaxy population is heterogenous, in qualitative agreement with several studies of IR-excess galaxies (e.g., Teplitz et al. 2007; Alexander et al. 2008; Murphy et al. 2009; Fadda et al. 2010; Georgakakis et al. 2010; Georgantopoulos et al. 2011).

3.1.3. X-Ray Spectral Analyses

To gain more insight into the intrinsic AGN properties (e.g., N_H, Γ, reflection components, Fe K emission) of the X-ray detected BzK galaxies, we fitted the X-ray data using physically motivated AGN models. Our main focus here is to constrain the X-ray spectral properties of the 11 heavily obscured AGNs to identify any potential Compton-thick AGN signatures (dominant reflection component; strong Fe K emission). However, we also explored the X-ray spectral properties of all of the X-ray detected BzK galaxies to provide constraints on key spectral parameters (e.g., the intrinsic X-ray spectral slope; Γ) and search for further heavily obscured AGNs not identified using the simple X-ray spectral slope criteria. We extracted the X-ray spectra of each source following Section 2.3 and initially fitted each X-ray spectrum over the observed-frame 0.5–8 keV energy band with an absorbed power-law model (the model components are WABS*ZWABS*POW in XSPEC) using the C statistic (Cash 1979).

We first focus on the results obtained for the nine luminous AGNs ($L_X > 10^{43}$ erg s^{-1}) since the good photon statistics ($\approx$220–4600 net counts; mean of $\approx$1600 net counts) provide accurate constraints on the intrinsic X-ray spectral slope and the presence of any absorption. The individual best-fitting parameters for the luminous AGNs are consistent with those expected for relatively unobscured AGNs ($\Gamma \approx 1.8$ and $N_H < 10^{23}$ cm^{-2}). To provide tighter overall constraints we also performed joint spectral fitting for all of the sources, which determines the best-fitting Γ and N_H for the whole sample. Jointly fitting Γ and N_H but leaving the normalization of each source to vary, we obtained $\Gamma = 1.71^{+0.03}_{-0.04}$ with low intrinsic absorption ($N_H = (0.65^{+0.06}_{-0.12}) \times 10^{22}$ cm^{-2}); the best-fitting parameters obtained from χ^2 fitting ($\Gamma = 1.78^{+0.04}_{-0.04}$ and $N_H = (0.79^{+0.15}_{-0.10}) \times 10^{22}$ cm^{-2}) are statistically consistent with those obtained using the C statistic. These constraints can help interpret the X-ray spectral properties of the heavily obscured AGNs. The results obtained for the 27 low-luminosity X-ray systems are similar to those obtained for the luminous AGNs but with considerably larger uncertainties ($\approx$3–180 net counts; mean of $\approx$30 net counts); the best-fitting parameters from
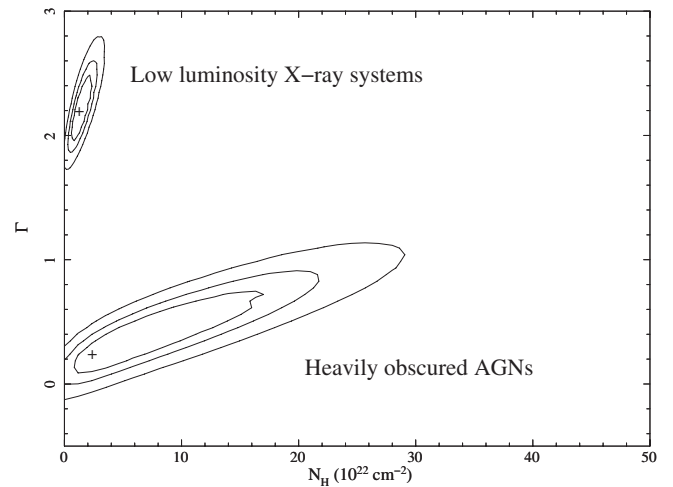
Figure 4. Best-fit parameters (Γ vs. N_H) from jointly fitting the X-ray spectra of the heavily obscured AGNs and low-luminosity X-ray systems with an absorbed power-law model. The contours refer to the 68%, 95%, and 99% confidence limits and the crosses indicate the best-fitting parameters. The best-fitting Γ for the heavily obscured AGNs is inconsistent with the intrinsic X-ray spectral slope found for AGN activity ($\Gamma \approx 1.3$–2.5; see Figure 2), suggesting that the observed X-ray emission for the overall sample is not well characterized by absorbed power-law emission.

jointly fitting the X-ray spectra are $\Gamma = 2.22^{+0.23}_{-0.29}$ with $N_H = (1.46^{+1.01}_{-0.47}) \times 10^{22}$ cm^{-2} (see Figure 4).

We now focus on the results obtained for the 11 heavily obscured AGNs. The only heavily obscured AGN that is bright enough for reasonable-quality individual X-ray spectral constraints is J033222.5–274603 ($\approx$560 net counts), which has $\Gamma = 0.93^{+0.28}_{-0.26}$ and $N_H = (0.82^{+0.41}_{-0.34}) \times 10^{23}$ cm^{-2}; the best-fitting parameters obtained from χ^2 fitting are $\Gamma = 1.03^{+0.26}_{-0.20}$ and $N_H = (1.80^{+0.58}_{-0.42}) \times 10^{23}$ cm^{-2}, with a reduced χ^2 of 1.13 for 24 degrees of freedom. The absorbing column density of this object suggests that it is Compton thin; however, the best-fitting X-ray spectral slope is flat. Examination of the residuals shows that the model significantly deviates from the data at observed-frame $<$1.5 keV. Fitting the X-ray data between observed-frame 1.5–8 keV gives $\Gamma = 1.40^{+0.30}_{-0.64}$ and $N_H = (2.05^{+0.97}_{-1.81}) \times 10^{23}$ cm^{-2}; the best-fitting parameters obtained from χ^2 fitting are $\Gamma = 1.59^{+0.52}_{-0.36}$ and $N_H = (2.68^{+1.66}_{-1.55}) \times 10^{23}$ cm^{-2}, with a reduced χ^2 of 1.03 for 20 degrees of freedom. These best-fitting parameters now provide a better characterization of the data and are consistent with that expected for an obscured Compton-thin AGN. The X-ray–8 μm luminosity ratio of $\approx$0.02 is also consistent with that expected for a Compton-thin AGN and is an order of magnitude larger than the luminosity ratio for the other heavily obscured AGNs (see Figure 3).

The best-fitting parameters for the other heavily obscured AGNs ($\approx$20–120 net counts; mean of $\approx$60 net counts) are determined from jointly fitting the X-ray spectra. Using the absorbed power-law model, the best-fitting parameters are $\Gamma = 0.35^{+0.43}_{-0.29}$ with $N_H = (5.79^{+12.34}_{-3.90}) \times 10^{22}$ cm^{-2}; see Figure 4. Such a flat intrinsic X-ray spectral slope is inconsistent with that found for typical AGNs and is also inconsistent with that expected from the inverse Compton scattering of accretion-disk photons (i.e., the X-ray emitting "corona"; Haardt & Maraschi 1993; Mushotzky et al. 1993; Reynolds & Nowak 2003). However, these properties are consistent with a reflection-dominated spectrum, such as that typically identified in Compton-thick AGNs and some heavily obscured Compton-thin AGNs (e.g.,

George & Fabian 1991; Matt et al. 1996, 2000; Ueda et al. 2007; Eguchi et al. 2009; Comastri et al. 2010). Indeed, from jointly fitting the X-ray spectra of the heavily obscured AGNs with a reflection-dominated spectrum (the PEXRAV model in XSPEC; Magdziarz & Zdziarski 1995), leaving the intrinsic X-ray spectral slope as the jointly fitted parameter but allowing the normalization of each source to vary, we obtain $\Gamma = 1.69^{+0.15}_{-0.07}$; the reflection parameter in PEXRAV is fixed to $R = -1$ (to produce only the reflection component), the cutoff energy is fixed to $E\_cut = 128$ keV (e.g., Malizia et al. 2003), and all of the other parameters (inclination angle, elemental abundances) are fixed at their default values. The best-fitting X-ray spectral slope is now in good agreement with that found for the luminous AGNs, providing evidence that these systems are the heavily obscured reflection-dominated counterparts of the luminous AGNs.

3.1.4. Reflection-dominated Heavily Obscured AGNs

To explore further whether the reflection-dominated model provides a good description of the X-ray spectra of the heavily obscured AGNs, we also produced a composite rest-frame 2–20 keV spectrum following Section 3.4 of Alexander et al. (2005a). Briefly, the unbinned spectrum of each object is fitted using a simple power-law model and an unfolded spectrum is produced, taking into account the *Chandra* effective area and exposure time. Each spectrum is then converted to rest-frame energies and all of the spectra are combined and binned to increase the signal-to-noise ratio. The composite X-ray spectrum of the heavily obscured AGNs is shown in Figure 5 and is compared to the PEXRAV model with $\Gamma = 1.7$. The similarity between the composite X-ray spectrum and the pure reflection model is striking, directly showing that the typical X-ray spectrum of the heavily obscured AGNs is reflection dominated. The composite X-ray spectrum is also consistent with that of reflection-dominated AGNs, such as those recently identified at $z \approx 0$ using >10 keV observatories (*Swift*; *Suzaku*; e.g., Ueda et al. 2007; Eguchi et al. 2009; Comastri et al. 2010); see Figure 5. The similarity between the composite spectrum of the low-luminosity X-ray sources and a $\Gamma = 2$ power-law spectrum suggests that many of these sources are either intrinsically weak AGNs (see Section 3.1.1 for X-ray variability constraints) or dominated by HMXBs; see Figure 2 for the typical range of X-ray spectral slopes for AGNs and HMXBs.

If the X-ray emission of the heavily obscured AGNs is dominated by reflection then we would also expect to identify strong Fe K emission (e.g., Reynolds & Nowak 2003). There is no clear evidence for Fe K emission in the stacked spectrum but since half of heavily obscured AGNs have photometric redshifts, the Fe K emission may be smeared out. To test this hypothesis we only stacked the X-ray spectra of the heavily obscured AGNs with spectroscopic redshifts; see the inset panel in Figure 5. Encouragingly, we now identify a strong emission feature (≈ 1 keV rest-frame equivalent width) at ≈ 6.4 keV, which is likely to be due to Fe K emission and suggests the presence of Compton-thick AGNs, which typically have Fe K emission with an equivalent width of $\gtrsim 1$ keV (e.g., George & Fabian 1991; Matt et al. 1996, 2000; Della Ceca et al. 2008). However, this feature is weaker (≈ 0.5 keV rest-frame equivalent width) when we remove J033235.7–274916, which has been individually identified with strong Fe K emission (Feruglio et al. 2011). Since Compton-thin AGNs have lower equivalent width Fe K emission than Compton-thick AGNs ($\lesssim 0.5$ keV; Mushotzky et al. 1993; Risaliti 2002; Dadina 2008), the weaker Fe K
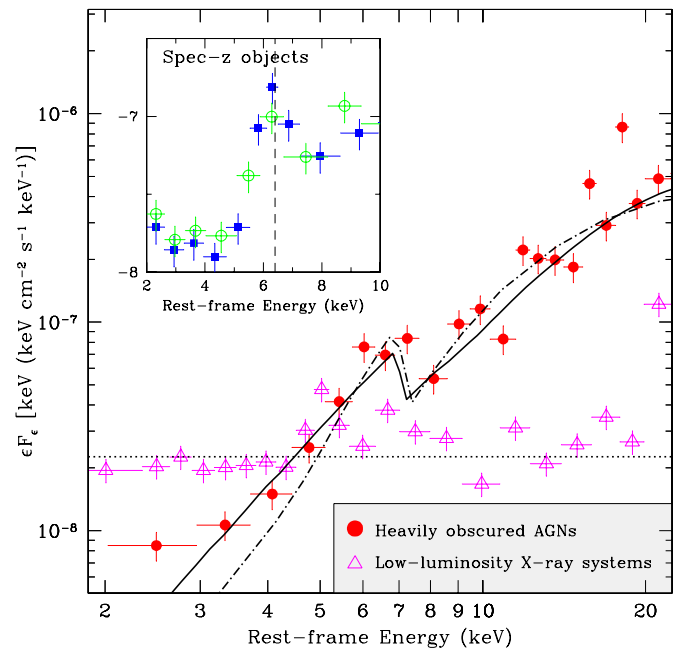
Figure 5. Flux density vs. rest-frame energy showing the composite rest-frame 2–20 keV spectra for the heavily obscured AGNs (filled circles; all objects except the X-ray bright AGN J033222.5–274603) and low-luminosity X-ray systems (open triangles) as compared to an unabsorbed power-law model (dotted line; $\Gamma = 2.0$), a pure reflection model (solid curve; $\Gamma = 1.7$), and the best-fitting model to the reflection-dominated $z \approx 0$ AGN *Swift* J0601.9–8636 (dot-dashed curve; Ueda et al. 2007); see Section 3.1.4. The inset panel shows the stacked X-ray spectra at rest-frame 2–10 keV of the heavily obscured AGNs with spectroscopic redshifts (filled squares: all objects; open circles: all objects except J033235.7–274916, which has been individually identified with Fe Kα emission; Feruglio et al. 2011); the dashed line shows the expected rest-frame energy of Fe Kα. The properties of the heavily obscured AGNs are consistent with those expected for reflection-dominated systems and $\approx 10\%$–50% are likely to be Compton-thick AGNs (see Section 3.1.4).

(A color version of this figure is available in the online journal.)

emission with J033235.7–274916 removed suggests that the heavily obscured AGNs comprise a combination of reflection-dominated Compton-thick and Compton-thin AGNs (e.g., Matt et al. 2000; Ueda et al. 2007; Eguchi et al. 2009; Comastri et al. 2010). Under the assumption that the Compton-thick AGNs have Fe K equivalent widths of $\gtrsim 1$ keV, this suggests that $\lesssim 50\%$ of the heavily obscured AGNs are absorbed by Compton-thick material; conversely, a lower limit to the Compton-thick AGN fraction is $\approx 10\%$ due to the identification of J033235.7–274916 (Feruglio et al. 2011). Qualitatively similar results have been obtained by Georgakakis et al. (2010) for IR-excess galaxies at $z \approx 1$.

Accurate measurements of the intrinsic X-ray luminosity are difficult in reflection-dominated AGNs due to large uncertainties on the reflecting geometry. We therefore employ several different approaches that should bracket the likely range in intrinsic X-ray luminosities. Clearly, a lower limit is obtained from the *observed* 2–8 keV luminosities, which gives an average luminosity of $\log(L_X/\mathrm{erg\,s^{-1}}) \approx 43.1$ at the average rest-frame energy of ≈ 6–24 keV. Conversely, an upper limit is obtained by assuming that the rest-frame 8 μm emission is dominated by AGN activity (i.e., on the basis of the AGN-dominated line in Figure 3); following this approach we obtain an average intrinsic X-ray luminosity of $\log(L_{2-10\,\mathrm{keV}}/\mathrm{erg\,s^{-1}}) \approx 44.0$ for the median rest-frame 8 μm luminosity of $\log(L_{8\,\mu\mathrm{m}}/L_\odot) \approx 11.1$. Lastly, we can estimate the intrinsic X-ray luminosity of the heavily obscured AGNs under the reasonable assumption that they are the
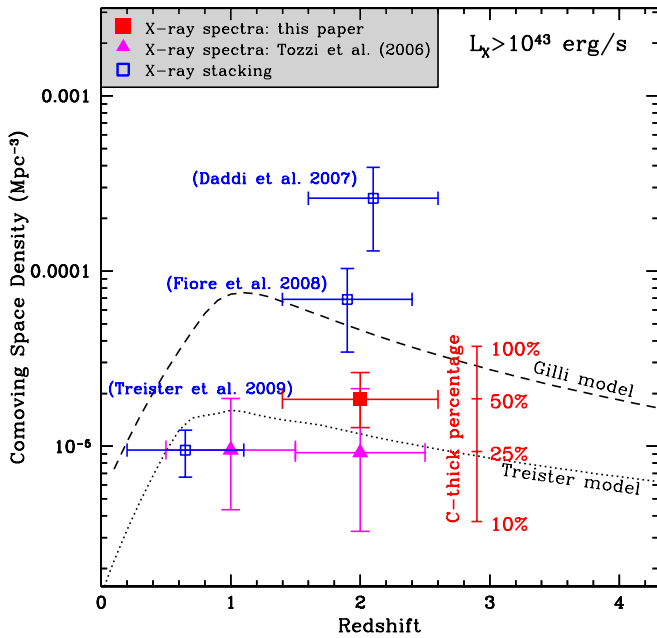
Figure 6. Space density of heavily obscured AGNs with $L_X \gtrsim 10^{43}$ erg s^{-1}. The plotted data only correspond to the results derived from the X-ray detected heavily obscured AGNs identified here (filled squares), candidate Compton-thick AGNs identified from X-ray spectral analyses in the CDF-S (filled triangles; Tozzi et al. 2006), and X-ray stacking analysis results of X-ray undetected candidate Compton-thick AGNs with $L_X \gtrsim 10^{43}$ erg s^{-1} (open squares; Daddi et al. 2007a; Fiore et al. 2008; Treister et al. 2009b). The solid bar indicates the space-density estimates for a range of Compton-thick AGN percentages for the heavily obscured AGNs identified here. These results are compared to the space-density predictions for Compton-thick AGNs with $L_X \gtrsim 10^{43}$ erg s^{-1} based on the models of Gilli et al. (2007; dashed curve) and Treister et al. (2009a; dotted curve).

(A color version of this figure is available in the online journal.)

absorbed counterparts of the luminous AGNs (see Section 3.1.3 for some evidence). Using the average X-ray–8 μm luminosity ratio of the luminous AGNs (≈ 0.07; a factor ≈ 3 less than the intrinsic ratio of ≈ 0.21), we estimate an average intrinsic luminosity for the heavily obscured AGNs of log($L_{2-10\,\mathrm{keV}}$/erg s^{-1}) ≈ 43.5. On the basis of this approach we predict a rest-frame 2–10 keV luminosity within a factor ≈ 2 of that measured from the optical and X-ray spectroscopy for the Compton-thick AGN J033235.7–274916 (Feruglio et al. 2011; see Figure 3), one of the heavily obscured AGNs in our sample. Since the average X-ray–8 μm luminosity ratio of the luminous AGNs is lower than that expected for AGN-dominated systems, a natural prediction of this final approach is that the rest-frame 8 μm emission from many of the heavily obscured AGNs is dominated by star formation activity, in agreement with that found from *Spitzer*-IRS spectroscopy (e.g., Murphy et al. 2009; Donley et al. 2010; Fadda et al. 2010).

3.2. X-Ray Undetected BzK Galaxies

The majority of the *BzK* galaxy population remains undetected in the 4 Ms *Chandra* observation (see Section 3.1) but may host X-ray weak AGN activity below the detection limit. We can place constraints on the presence of heavily obscured AGN activity in these systems using X-ray stacking analyses. We stacked the X-ray data of the X-ray undetected *BzK* galaxies adopting the procedure in Section 2.5. The X-ray stacking results are presented in Table 3. As previously found from the X-ray stacking analyses of *BzK* galaxies in Daddi et al. (2007a),

the result for the IR-excess galaxies differs from that of the IR-normal galaxies: $\Gamma = 1.4^{+0.3}_{-0.3}$ for the IR-excess galaxies and $\Gamma = 2.0^{+0.4}_{-0.4}$ for the IR-normal galaxies; see Table 3. The stacked X-ray spectral slope for the IR-normal galaxies is consistent with that found by Daddi et al. (2007a) using the 1 Ms *Chandra* data ($\Gamma \approx 1.8$) but the X-ray spectral slope for the IR-excess galaxies is significantly steeper ($\Gamma \approx 0.9$ was obtained by Daddi et al. 2007a).

The lack of a flat X-ray spectral slope for the IR-excess galaxies appears to suggest that we have now individually detected many of the heavily obscured AGNs that were originally contributing to the stacked data in Daddi et al. (2007a). However, we must be careful when interpreting X-ray stacking analyses of X-ray undetected source populations, since the effects of Eddington bias and source variability (see Section 3.1.1) can dominate over the X-ray signal produced by the majority of the source population. For example, in going from the 1 Ms *Chandra* data to the 4 Ms *Chandra* data, the same number of heavily obscured AGNs were identified in the IR-excess (3 of the 13 X-ray detected sources) and IR-normal (3 of the 14 X-ray detected sources) galaxy populations despite there being little evidence for heavily obscured AGNs in the IR-normal galaxies from the 1 Ms stacked data of Daddi et al. (2007a). It is therefore likely that further heavily obscured AGNs will be identified with deeper *Chandra* data but we cannot provide direct X-ray constraints from the current data set.

3.3. Re-evaluation of the Space Density of Distant Compton-thick AGNs

Distant Compton-thick AGNs are of great scientific interest since they may produce a large fraction of the unresolved > 8 keV background (e.g., Worsley et al. 2005; Gilli et al. 2007; Treister et al. 2009a). In Section 3.1 we used a variety of analyses (strong reflected-dominated spectrum, identification of Fe K, small X-ray–8 μm luminosity ratios) to infer that $\approx 10\%$–50% of the X-ray detected heavily obscured AGNs are Compton thick; the lower limit on the Compton-thick AGN fraction corresponds to the clear identification of the Compton-thick AGN in J033235.7–274916 (Feruglio et al. 2011), while the upper limit corresponds to the constraints derived from the stacked X-ray spectrum when J033235.7–274916 is removed. We can use these constraints to better estimate the space density of distant Compton-thick AGNs. In this calculation we have assumed a broad redshift range of $z = 1.4$–2.6, which gives a comoving volume of ≈ 0.7 Gpc^3 for the 5.5 arcmin radius region explored here. We have taken into account the 10% incompleteness in the *BzK* galaxy selection due to blended *Spitzer*-IRAC sources and the 30% incompleteness due to unreliable UV slopes (see Section 5.1 in Daddi et al. 2007a).

Following the procedure outlined above, we calculate a Compton-thick AGN space density of $\Phi_{\mathrm{C\text{-}thick}} \approx f \times 4 \times 10^{-5}$ Mpc^{-3} at $z \approx 1.4$–2.6, where f corresponds to the Compton-thick AGN fraction in our heavily obscured AGN sample; see Figure 6. As argued in Section 3.1.4, the average intrinsic X-ray luminosity of these heavily obscured AGNs is $L_{2-10\,\mathrm{keV}} \gtrsim 10^{43}$ erg s^{-1}. Although undoubtedly uncertain, our most optimistic space-density estimates lie below the constraints derived from X-ray stacking analyses of X-ray undetected IR-bright galaxy populations (Daddi et al. 2007a; Fiore et al. 2008): our space-density estimates are $\gtrsim 10$ times lower than those of Daddi et al. (2007a), who used the same object-selection approach as that adopted here but relied only on X-ray stacking analyses of X-ray undetected galaxies. Our

Table 3
X-Ray Stacking Analyses of the X-Ray Undetected BzK Galaxies

Sample	N	z[a]	L_{UV} $\log(L_\odot)$[a]	$vL_{8\mu m}$ $\log(L_\odot)$[a]	0.5–2 keV $(10^{-6}$ counts s$^{-1})$[b]	2–8 keV $(10^{-6}$ counts s$^{-1})$[b]	Band Ratio[c]	Γ[c]	$L_{2-10 keV}$ $\log(\text{erg s}^{-1})$[d]
IR excess galaxies: $K < 22$	47	1.97 ± 0.34	11.45 ± 0.46	11.01 ± 0.33	1.47 (12.6)	0.84 (3.9)	0.57 ± 0.15	1.4 ± 0.3	41.40
IR normal galaxies: $K < 22$	116	1.93 ± 0.44	11.48 ± 0.26	10.53 ± 0.30	1.19 (15.8)	0.42 (2.8)	0.33 ± 0.12	2.0 ± 0.4	41.32

Notes.

[a] Median galaxy properties and MAD (see Footnote "18"): redshift, extinction-corrected UV luminosity (rest-frame 1500 Å see Section 3.6 of Daddi et al. 2007b), rest-frame 8 μm luminosity (calculated using the 24 μm flux density, with small K-corrections applied; see Section 3.1 of Daddi et al. 2007b).

[b] Count rates in the 0.5–2 keV and 2–8 keV bands; the numbers in parentheses correspond to the S/N.

[c] X-ray spectral properties: band ratio (2–8 keV to 0.5–2 keV count-rate ratio) and X-ray spectral slope (Γ), derived from the band ratio, and 1σ uncertainties. Calculated following Xue et al. (2011).

[d] Rest-frame 2–10 keV luminosity calculated from the 0.5–2 keV flux and converted to rest-frame 2–10 keV assuming $\Gamma = 1.8$; the 0.5–2 keV flux is calculated following Xue et al. (2011).

space-density constraints are also broadly consistent with those of Tozzi et al. (2006), who identified reflection-dominated AGNs using X-ray spectral analyses of sources detected in the 1 Ms CDF-S observations; we have plotted the Tozzi et al. (2006) space density in Figure 5 assuming that 100% of the reflection-dominated AGNs are Compton thick and therefore this represents the maximum space density from that study. However, our space-density estimate is also a lower limit on the true Compton-thick AGN space density since (1) there may be further Compton-thick AGNs with intrinsic $L_{2-10 keV} \gtrsim 10^{43}$ erg s^{-1} that lie below our X-ray detection limit (i.e., those with $N_H \gg 10^{24}$ cm^{-2} and a weak reflection component; e.g., Matt et al. 2000) and (2) our sample does not include distant Compton-thick AGNs not selected using the BzK technique. An example of the latter is the $z = 1.53$ X-ray bright AGN CXO J033218.3–275055, which has strong Fe K emission identified in the 3 Ms *XMM-Newton* observations of the CDF-S (Comastri et al. 2011) but is not selected as a BzK galaxy.[20] A more complete AGN selection can be derived using mid-to-far-infrared selection, which is the focus of a future paper (A. Del Moro et al. 2011, in preparation).

Many studies have predicted the space density of distant Compton-thick AGNs from the X-ray luminosity functions of relatively unobscured AGNs and X-ray background constraints (see Ballantyne et al. 2011 for a comparison of many of the current studies). In Figure 6 we compare our space-density constraints with the predictions from Gilli et al. (2007) and Treister et al. (2009a) for $L_X \gtrsim 10^{43}$ erg s^{-1}, which broadly represent the most optimistic and pessimistic estimates, respectively. The model predictions are already in broad agreement with our range of space-density measurements, despite our conservative source-selection approach. However, given the significant uncertainties in the fraction of Compton-thick AGNs and sample incompleteness, strong conclusions cannot be derived from the current data.

We can also compare our derived Compton-thick AGN space density to constraints for other distant AGN populations. From a variety of studies, the measured space density of $L_X \gtrsim 10^{43}$ erg s^{-1} AGNs at $z \approx 2$ ranges from $\approx(1-2) \times 10^{-5}$ Mpc^{-3} for unobscured AGNs ($N_H < 10^{22}$ cm^{-2}) to $\approx(1-7) \times 10^{-5}$ Mpc^{-3} for all AGNs (e.g., Barger et al. 2005; Hasinger et al. 2005; La Franca et al. 2005; Silverman et al. 2008; Aird et al. 2010). On the basis of these studies, our constraints imply that the space density of Compton-thick

AGNs at $z \approx 2$ is comparable to that of unobscured AGNs at $z \approx 2$ and also suggests that Compton-thick AGNs comprise a non-negligible fraction of the AGN population at $z \approx 2$. However, our constraints do not yet support the hypothesis that Compton-thick AGNs outnumber Compton-thin AGNs at high redshift. The direct identification of individual Compton-thick AGN signatures from X-ray, optical, and mid-IR spectroscopy (e.g., Alexander et al. 2008; Comastri et al. 2011; Feruglio et al. 2011; Goulding et al. 2011) in a statistically significant number of objects ($\gtrsim$10–20 objects) are required to provide more reliable constraints. New facilities such as *NuSTAR* (high-energy 6–78 keV imaging; Harrison et al. 2010) and *JWST* (optical–mid-IR spectroscopy; Gardner et al. 2006) may also provide improved constraints, along with deeper *Chandra*/*XMM-Newton* observations and future proposed X-ray observatories such as *WFXT* (Murray et al. 2010).

4. SUMMARY

We have used the 4 Ms *Chandra* Deep Field-South observation to constrain the ubiquity of heavily obscured AGNs in the $z \approx 2$ BzK galaxy population. Our main results are as follows.

1. Forty-seven of the 222 BzK galaxies are X-ray detected in the central region of the 4 Ms CDF-S field: 11 are heavily obscured AGNs ($\Gamma \lesssim 1$), 9 are luminous AGNs ($L_X \gtrsim 10^{43}$ erg s^{-1}), and 27 are low-luminosity X-ray systems (relatively unobscured AGNs and starburst galaxies). Thirteen ($\approx$48%) of the 27 X-ray detected BzK galaxies with reasonable-quality X-ray data (> 20 counts in the 0.5–8 keV band) are found to be variable in the X-ray band, including six luminous AGNs, four heavily obscured AGNs, and three low-luminosity X-ray sources. See Sections 2.2, 2.4, and 3.1.1.

2. The overall X-ray spectra of the heavily obscured AGNs are better characterized by a pure reflection model than an absorbed power-law model, suggesting extreme Compton-thick absorption ($N_H \gtrsim 10^{24}$ cm^{-2}) in many systems. The identification of an emission-line feature at rest-frame $\approx$6.4 keV in the composite 2–20 keV spectrum and the small X-ray–8 μm luminosity ratios for the majority of these systems provide further support for this interpretation. See Sections 3.1.2–3.1.4.

3. Many of the heavily obscured AGNs are IR-excess galaxies. However, only $\approx$25% of the X-ray detected IR-excess galaxies are heavily obscured AGNs, which is otherwise composed of relatively unobscured AGNs and starburst galaxies. See Section 3.1.2.

---

[20] We also note as an aside that only 5 ($\approx$45%) of the 11 X-ray detected heavily obscured AGNs would be selected using the Fiore et al. (2008) selection criteria of $R - K > 4.5$ and $f_{24\mu m}/f_R > 1000$.

4. X-ray stacking analyses of the X-ray undetected BzK galaxies do not clearly reveal the presence of further X-ray undetected AGNs below the *Chandra* detection limit. This does not rule out the possibility that many other heavily obscured AGNs will be detected with deeper X-ray observations but it does suggest that they are not the dominant X-ray undetected population. See Sections 2.5 and 3.2.

5. We estimate a Compton-thick AGN space density of $\Phi_{\text{C-thick}} \approx f \times 4 \times 10^{-5}$ Mpc^{-3} at $z \approx 1.4$–2.6, where f lies between ≈ 0.1 and 0.5. Although highly uncertain, these constraints are already consistent with the range of predictions from X-ray background models and imply that the space density of Compton-thick AGNs at $z \approx 2$ is comparable to that of unobscured AGNs at $z \approx 2$. See Sections 3.1.4 and 3.3.

REFERENCES

Aird, J., et al. 2010, MNRAS, 401, 2531
Alexander, D. M., Bauer, F. E., Chapman, S. C., Smail, I., Blain, A. W., Brandt, W. N., & Ivison, R. J. 2005a, ApJ, 632, 736
Alexander, D. M., Chartas, G., Bauer, F. E., Brandt, W. N., Simpson, C., & Vignali, C. 2005b, MNRAS, 357, L16
Alexander, D. M., et al. 2003, AJ, 126, 539
Alexander, D. M., et al. 2008, ApJ, 687, 835
Appenzeller, I., et al. 1998, Messenger, 94, 1
Avni, Y. 1976, ApJ, 210, 642
Balestra, I., et al. 2010, A&A, 512, A12
Ballantyne, D. R., Draper, A. R., Madsen, K. K., Rigby, J. R., & Treister, E. 2011, ApJ, in press (arXiv:1105.0965)
Barger, A. J., Cowie, L. L., Mushotzky, R. F., Yang, Y., Wang, W.-H., Steffen, A. T., & Capak, P. 2005, AJ, 129, 578
Bassani, L., Dadina, M., Maiolino, R., Salvati, M., Risaliti, G., della Ceca, R., Matt, G., & Zamorani, G. 1999, ApJS, 121, 473
Bauer, F. E., Yan, L., Sajina, A., & Alexander, D. M. 2010, ApJ, 710, 212
Berghea, C. T., Weaver, K. A., Colbert, E. J. M., & Roberts, T. P. 2008, ApJ, 687, 471
Brandt, W. N., & Alexander, D. M. 2010, Publ. Natl Acad. Sci., 107, 7184
Brandt, W. N., & Hasinger, G. 2005, ARA&A, 43, 827
Broos, P. S., Townsley, L. K., Feigelson, E. D., Getman, K. V., Bauer, F. E., & Garmire, G. P. 2010, ApJ, 714, 1582
Brusa, M., et al. 2009, ApJ, 693, 8
Burlon, D., Ajello, M., Greiner, J., Comastri, A., Merloni, A., & Gehrels, N. 2010, ApJ, 728, 58
Cardamone, C. N., et al. 2010, ApJS, 189, 270
Cash, W. 1979, ApJ, 228, 939
Cimatti, A., et al. 2008, A&A, 482, 21
Comastri, A. 2004, in Supermassive Black Holes in the Distant Universe, ed. A. J. Barger (Astrophysics and Space Science Library, Vol. 308; Dordrecht: Kluwer), 245
Comastri, A., Iwasawa, K., Gilli, R., Vignali, C., Ranalli, P., Matt, G., & Fiore, F. 2010, ApJ, 717, 787
Comastri, A., et al. 2011, A&A, 526, L9
Daddi, E., Cimatti, A., Renzini, A., Fontana, A., Mignoli, M., Pozzetti, L., Tozzi, P., & Zamorani, G. 2004, ApJ, 617, 746
Daddi, E., et al. 2007a, ApJ, 670, 173
Daddi, E., et al. 2007b, ApJ, 670, 156
Dadina, M. 2008, A&A, 485, 417
Della Ceca, R., et al. 2008, Mem. Soc. Astron. Ital., 79, 65
Donley, J. L., Rieke, G. H., Alexander, D. M., Egami, E., & Pérez-González, P. G. 2010, ApJ, 719, 1393
Donley, J. L., Rieke, G. H., Pérez-González, P. G., & Barro, G. 2008, ApJ, 687, 111
Eguchi, S., Ueda, Y., Terashima, Y., Mushotzky, R., & Tueller, J. 2009, ApJ, 696, 1657
Fabian, A. C. 1999, MNRAS, 308, L39
Fadda, D., et al. 2010, ApJ, 719, 425
Feruglio, C., Daddi, E., Fiore, F., Alexander, D. M., Piconcelli, E., & Malacaria, C. 2011, ApJ, 729, L4
Fiore, F., et al. 2008, ApJ, 672, 94
Fiore, F., et al. 2009, ApJ, 693, 447
Gandhi, P., Horst, H., Smette, A., Hönig, S., Comastri, A., Gilli, R., Vignali, C., & Duschl, W. 2009, A&A, 502, 457
Gardner, J. P., et al. 2006, Space Sci. Rev., 123, 485
Georgakakis, A., Rowan-Robinson, M., Nandra, K., Digby-North, J., Pérez-González, P. G., & Barro, G. 2010, MNRAS, 406, 420
Georgantopoulos, I., Akylas, A., Georgakakis, A., & Rowan-Robinson, M. 2009, A&A, 507, 747
Georgantopoulos, I., Georgakakis, A., Rowan-Robinson, M., & Rovilos, E. 2008, A&A, 484, 671
Georgantopoulos, I., Rovilos, E., Xilouris, E. M., Comastri, A., & Akylas, A. 2011, A&A, 526, A86
George, I. M., & Fabian, A. C. 1991, MNRAS, 249, 352
Gibson, R. R., Brandt, W. N., & Schneider, D. P. 2008, ApJ, 685, 773
Gilfanov, M. 2010, The Jet Paradigm (Lecture Notes in Physics, Vol. 794; Berlin: Springer), 17
Gilfanov, M., Grimm, H., & Sunyaev, R. 2004, MNRAS, 351, 1365
Gilli, R., Comastri, A., & Hasinger, G. 2007, A&A, 463, 79
Gilli, R., Vignali, C., Mignoli, M., Iwasawa, K., Comastri, A., & Zamorani, G. 2010, A&A, 519, A92
Goulding, A. D., Alexander, D. M., Mullaney, J. R., Gelbord, J. M., Hickox, R. C., Ward, M., & Watson, M. G. 2011, MNRAS, 411, 1231
Granato, G. L., Silva, L., Lapi, A., Shankar, F., De Zotti, G., & Danese, L. 2006, MNRAS, 368, L72
Grazian, A., et al. 2006, A&A, 449, 951
Guainazzi, M., Matt, G., & Perola, G. C. 2005, A&A, 444, 119
Haardt, F., & Maraschi, L. 1993, ApJ, 413, 507
Harrison, F. A., et al. 2010, Proc. SPIE, 7732, 21
Hasinger, G. 2008, A&A, 490, 905
Hasinger, G., Miyaji, T., & Schmidt, M. 2005, A&A, 441, 417
Heckman, T. M., Ptak, A., Hornschemeier, A., & Kauffmann, G. 2005, ApJ, 634, 161
Hickox, R. C., & Markevitch, M. 2006, ApJ, 645, 95
Hopkins, P. F., Hernquist, L., Cox, T. J., Di Matteo, T., Robertson, B., & Springel, V. 2006, ApJS, 163, 1
Iwasawa, K., Sanders, D. B., Evans, A. S., Mazzarella, J. M., Armus, L., & Surace, J. A. 2009, ApJ, 695, L103
Kim, D.-W., Fabbiano, G., & Trinchieri, G. 1992, ApJS, 80, 645
Krabbe, A., Böker, T., & Maiolino, R. 2001, ApJ, 557, 626
La Franca, F., et al. 2005, ApJ, 635, 864
Le Fèvre, O., et al. 2003, Proc. SPIE, 4841, 1670
Lehmer, B. D., et al. 2005, AJ, 129, 1
Lehmer, B. D., et al. 2008, ApJ, 681, 1163
Luo, B., et al. 2010, ApJS, 187, 560
Lutz, D., Maiolino, R., Spoon, H. W. W., & Moorwood, A. F. M. 2004, A&A, 418, 465
Lutz, D., Sturm, E., Genzel, R., Spoon, H. W. W., Moorwood, A. F. M., Netzer, H., & Sternberg, A. 2003, A&A, 409, 867
Magdziarz, P., & Zdziarski, A. A. 1995, MNRAS, 273, 837
Maiolino, R., Salvati, M., Bassani, L., Dadina, M., della Ceca, R., Matt, G., Risaliti, G., & Zamorani, G. 1998, A&A, 338, 781
Malizia, A., Bassani, L., Stephen, J. B., Di Cocco, G., Fiore, F., & Dean, A. J. 2003, ApJ, 589, L17
Maronna, R. A., Martin, R. D., & Yohai, V. J. 2006, Robust Statistics: Theory and Methods (1st ed.; Chichester: Wiley)
Matt, G., Brandt, W. N., & Fabian, A. C. 1996, MNRAS, 280, 823
Matt, G., Fabian, A. C., Guainazzi, M., Iwasawa, K., Bassani, L., & Malaguti, G. 2000, MNRAS, 318, 173
Matt, G., et al. 1997, A&A, 325, L13
McCracken, H. J., et al. 2010, ApJ, 708, 202

Mignoli, M., et al. 2005, A&A, 437, 883

Mullaney, J. R., Alexander, D. M., Huynh, M., Goulding, A. D., & Frayer, D. 2010, MNRAS, 401, 995

Murphy, E. J., Chary, R. R., Alexander, D. M., Dickinson, M., Magnelli, B., Morrison, G., Pope, A., & Teplitz, H. I. 2009, ApJ, 698, 1380

Murphy, K. D., & Yaqoob, T. 2009, MNRAS, 397, 1549

Murray, S. S., et al. 2010, Proc. SPIE, 7732, 58

Mushotzky, R. F., Done, C., & Pounds, K. A. 1993, ARA&A, 31, 717

Nandra, K., George, I. M., Mushotzky, R. F., Turner, T. J., & Yaqoob, T. 1997, ApJ, 476, 70

Nandra, K., & Pounds, K. A. 1994, MNRAS, 268, 405

Nenkova, M., Sirocky, M. M., Nikutta, R., Ivezić, Ž., & Elitzur, M. 2008, ApJ, 685, 160

Nousek, J. A., & Shue, D. R. 1989, ApJ, 342, 1207

Paolillo, M., Schreier, E. J., Giacconi, R., Koekemoer, A. M., & Grogin, N. A. 2004, ApJ, 611, 93

Popesso, P., et al. 2009, A&A, 494, 443

Ptak, A., Serlemitsos, P., Yaqoob, T., & Mushotzky, R. 1999, ApJS, 120, 179

Rafferty, D. A., Brandt, W. N., Alexander, D. M., Xue, Y. Q., Bauer, F. E., Lehmer, B. D., Luo, B., & Papovich, C. 2011, ApJ, submitted

Ranalli, P., Comastri, A., & Setti, G. 2003, A&A, 399, 39

Reynolds, C. S., & Nowak, M. A. 2003, Phys. Rep., 377, 389

Rigopoulou, D., Spoon, H. W. W., Genzel, R., Lutz, D., Moorwood, A. F. M., & Tran, Q. D. 1999, AJ, 118, 2625

Risaliti, G. 2002, A&A, 386, 379

Risaliti, G., Maiolino, R., & Salvati, M. 1999, ApJ, 522, 157

Shao, L., et al. 2010, A&A, 518, L26

Silverman, J. D., et al. 2008, ApJ, 679, 118

Stark, A. A., Gammie, C. F., Wilson, R. W., Bally, J., Linke, R. A., Heiles, C., & Hurwitz, M. 1992, ApJS, 79, 77

Steffen, A. T., Strateva, I., Brandt, W. N., Alexander, D. M., Koekemoer, A. M., Lehmer, B. D., Schneider, D. P., & Vignali, C. 2006, AJ, 131, 2826

Szokoly, G. P., et al. 2004, ApJS, 155, 271

Teplitz, H. I., et al. 2007, ApJ, 659, 941

Tozzi, P., et al. 2006, A&A, 451, 457

Treister, E., & Urry, C. M. 2006, ApJ, 652, L79

Treister, E., Urry, C. M., & Virani, S. 2009a, ApJ, 696, 110

Treister, E., et al. 2006, ApJ, 640, 603

Treister, E., et al. 2009b, ApJ, 706, 535

Ueda, Y., et al. 2007, ApJ, 664, L79

Vanzella, E., et al. 2008, A&A, 478, 83

Vignali, C., Alexander, D. M., Gilli, R., & Pozzi, F. 2010, MNRAS, 404, 48

Vignali, C., Brandt, W. N., & Schneider, D. P. 2003, AJ, 125, 433

Vignati, P., et al. 1999, A&A, 349, L57

Wolk, S. J., et al. 2008, Proc. SPIE, 7011, 88

Worsley, M. A., et al. 2005, MNRAS, 357, 1281

Xue, Y. Q., et al. 2010, ApJ, 720, 368

Xue, Y. Q., et al. 2011, ApJS, 195, 10

Yaqoob, T., Murphy, K. D., Miller, L., & Turner, T. J. 2010, MNRAS, 401, 411